Structure and magnetic properties of epitaxial cobalt islands

M. Demand[1], M. Hehn[2,a], R.L. Stamps[3], C. Meny[1], and K. Ounadjela[1]

[1] Institut de Physique et de Chimie des Matériaux de Strasbourg, 23 rue du Loess, 67037 Strasbourg Cedex, France
[2] Laboratoire de Physique des Matériaux[b], BP 239, 54506 Vandœuvre-lès-Nancy Cedex, France
[3] Department of Physics, University of Western Australia, Nedlands, WA 6907, Australia

Abstract. Growth, structural and magnetic properties of cobalt island structures grown by molecular beam epitaxy on 4 nm thick island shaped Ru buffers are studied. The islands are characterized by a narrow distribution of sizes, and are separated on average by spacing of around one hundred nanometers. Growth of the islands into continuous films is found to proceed in three well defined stages, and corresponding magnetic behaviors are identified. The particles formed in the first stage of growth appear to be similar in shape and size, and their magnetic behavior suggest the presence of superparamagnetism. Particles in the second stage of growth are ferromagnetic and display a reorientation transition of their magnetization out of the film plane, consistent with that seen in patterned magnetic dot arrays. Particles coalesce in the last stage of growth and magnetic properties of continuous films are observed.

PACS. 75.50.Tt Fine-particle systems; nanocrystalline materials – 75.30.Gw Magnetic anisotropy – 75.60-d Domain effects, magnetization curves, and hysteresis

1 Introduction

Nanometer structured magnetic materials are of great interest for studies of mesoscopic magnetism and also for their potential technological applications as high-density magnetic storage media. In those systems, the key parameter is the exchange length, L_{ex}, which is typically of the order of ten nanometers. Reducing the lateral size of dots to L_{ex} has a strong influence on the micromagnetic domain configuration and can lead to single domain particles suitable to storage media. However, reducing dimensions to submicron scale with a high reproducibility and well defined shapes is a technical challenge and therefore several fabrication methods have been proposed. Most current preparation techniques are mainly based on costly and complex lithographic processes usually combined with etching and lift-off techniques [1–3]. Thus, techniques allowing the direct growth of nanostructures have been developed. It is possible to fabricate arrays of nanometric structures grown on vicinal surfaces [4,5], dislocation networks [6], or reconstructed surfaces [7,8]. Other alternative techniques have also been developed, as for example electrochemically grown wires in pore of membranes [9], and self-organized islands and line networks grown *via* a patterned template [10]. The growth of magnetic particles deposited on a non metallic structured substrate have been reported previously by Ohnuma *et al.* [11]. This

method uses a sputter etched polymer substrate to provide an islanding-shape buffer which supports magnetic particle growth.

In this paper, a method is examined for producing arrays of magnetic particles based on island growth on a substrate. The arrays considered here are Co islands grown by molecular beam epitaxy on an island shaped Ru buffer layer. An optimized Ru thickness was found that resulted in a structured buffer layer that forced subsequent Co film deposition to form separated small particles. By increasing the Co nominal deposited thickness, a thin Co film forms covered by Co islands with a narrow distribution of size. Finally, for very thick films, a transition between a columnar structure and a negative columnar structure (*i.e.* a continuous film pierced by holes) was observed [12]. The ability to vary the roughness is useful in order to study how film roughness affects magnetic properties and the exploration of the relationship between roughness and magnetic properties is the main topic of this work. We concentrate here on the early stages of Co island growth and on their magnetic properties which differs considerably from the one observed for flat or rough thick layers obtained after island coalescence [12,14].

The key point to understand this process is to try to establish correlations between the growth modes (continuous layer or formation of islands) and the magnetic properties of the samples. To address this question we studied the film structure as a function of thickness using Atomic Force Microscopy (AFM). Then we tried to correlate these results with microscopic magnetic properties

[a] e-mail: `hehn@lpm.u-nancy.fr`
[b] UMR CNRS 7556

measured using Magnetic Force Microscopy (MFM), and with macroscopic magnetic properties using Alternating Gradient Field Magnetometry (AGFM). In addition, measurements of magnetic anisotropy were also performed by using a variable temperature torque magnetometer. The paper is organized as follows. In Section 2 the growth and structure of the films are examined and growth modes are proposed based on extensive AFM analysis. To our knowledge no AFM investigation of Ru film topography in the thickness range examined here has been reported before. Section 3 contains a description of observed magnetic properties with an emphasis on anisotropy temperature dependencies. Details of a spin reorientation are reported in Section 4. A summary and conclusion are provided in Section 5.

2 Fabrication, growth modes and structural characterization

In this study, Ru/Co/Ru trilayers have been grown by ultra high vacuum e-beam epitaxy in a chamber with a base pressure of 10^{-10} torr. The distance between the sample and the e-gun was set to 20 cm to avoid bombardment of the substrate by fast ions/electrons. The deposition process is as follows. A rough 4 nm thick Ru buffer layer was first grown at 700 °C with a flux of 0.05 Å/s on freshly cleaved mica substrates in order to initiate an 'islanding' hcp (0001) growth of Co. Next, the substrate is cooled down and the Co layer was grown at 500 °C with a flux of 0.2 Å/s. Finally, all the samples were capped with a 2 nm thick Ru layer to prevent oxidation. The growth parameters, and especially the substrate temperature during deposition, have been optimized in previous studies [15] to get the best hcp (0001) crystalline structure of the Ru and Co layers with the c axis perpendicular to the film plane. By stabilizing a (0001) hcp cobalt structure which gives rise to a large perpendicular magnetocrystalline anisotropy ($K_{MC,hcp} = 5.2 \times 10^6$ erg cm^{-3}), domains with magnetization perpendicular to the film plane are favored [14]. Therefore, only the thickness of the Ru layer was varied to get 'islanding' of the Co layer, the growth temperature and the flux were kept constant. Growth and island formation during the Ru and Co phases are described below.

2.1 Ruthenium buffer layer growth

The surface topography of the Ru buffer was examined for different nominal deposited thickness using an Atomic Force Microscope (AFM). This allows the determination of an optimal Ru thickness for islanding growth of Co. Twenty Ru films were deposited on a mica substrate with a nominal Ru thickness (t_{Ru}), the thickness of the Ru layer when it is continuous, ranging from 1 nm to 20 nm. The deposition temperature was fixed to 700 °C to allow a large surface diffusion of the Ru on mica to favor an hcp(0001) structure of the film.
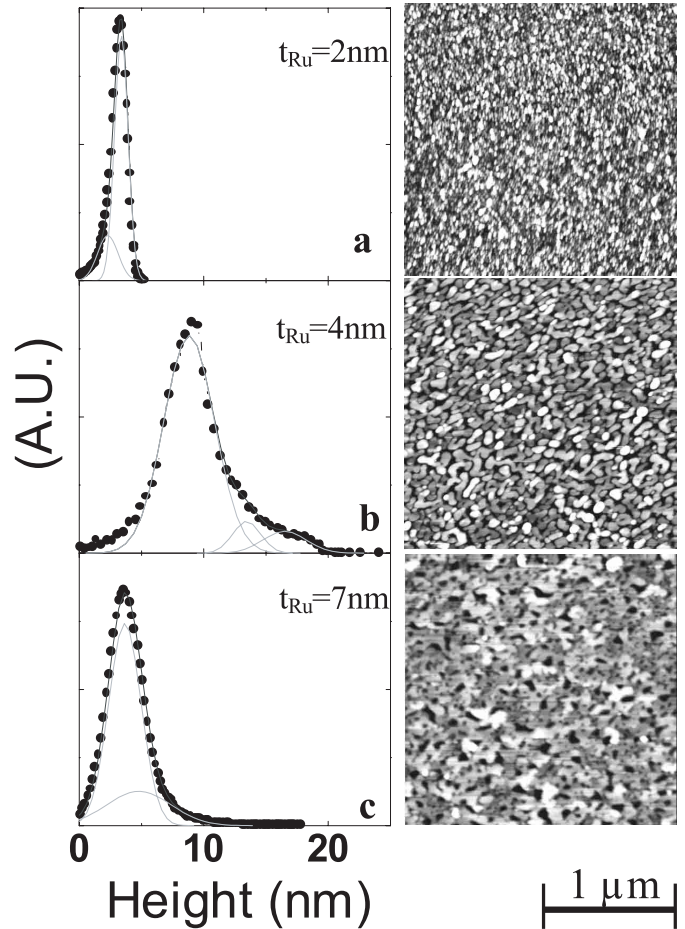

Fig. 1. AFM topographic images (2μm $\times$ 2μm in size)of the Ru buffer layer for different stages of its growth and corresponding height distributions for $t_{Ru} = 2$ nm (a), $t_{Ru} = 4$ nm (b) and $t_{Ru} = 7$ nm (c). The height distributions (solid circles) have been fitted using a combination of Gaussian functions indicated by the thin lines.

During the growth process, the Ru appears to follow the same surface morphological phases as observed in the case of Ag on mica [16,17]. In the early stages of growth, homogeneous nucleation takes place. Islands have a narrow distribution of thickness as well as a narrow distribution of lateral size and lateral spacing in the array. As can be seen in Figure 1a, the topography for $t_{Ru} = 2$ nm exhibits a high density of small closely packed particles with lateral dimensions ranging typically from 20 nm to 60 nm, and an average height of about 3 nm. The height distributions were fitted using a combination of two or more Gaussian functions (thin lines in Fig. 1). That way, the contribution of different families of particles can be extracted. The slight asymmetry in the measured distribution suggests that there is a small contribution from islands between 1 and 2 nm height, but the majority are clearly centered around a height of 3 nm. The nearest Ru patches merge and increase in height as the Ru thickness is increased. This means that the three dimensions of the islands increase with increasing nominal film thickness.
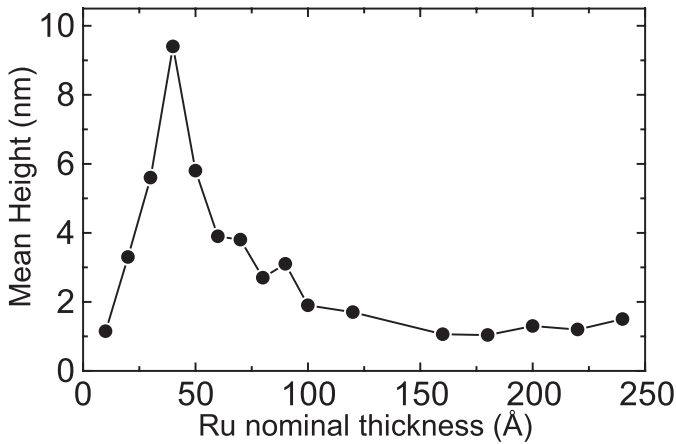
Fig. 2. Evolution of the mean island height determined from the AFM images *versus* Ru nominal film thickness.

For $t_{Ru} = 4$ nm, the AFM image (Fig. 1b) shows a coexistence of isolated islands and irregular channels which result from islands that have already coalesced. A higher Ru coverage leads to an interconnecting structure with long irregular channels. Indeed, increasing the thickness of the Ru buffer from 4 nm to 5 nm reduces its resistance from an infinite to a finite value: percolation of the islands occurs in this thickness range. Those channels are approximately 100 nm to 200 nm in width and 6 nm in depth. A further increase of the Ru thickness induces the channels to fill in. For $t_{Ru} = 7$ nm, the buffer layer becomes essentially a continuous film pierced by holes (Fig. 1c). The holes are about 20 nm to 90 nm in diameter and 4 nm in depth. Finally, a smooth surface with a peak to peak roughness of about 1 to 1.5 nm is obtained for Ru thicknesses above 15 nm.

One parameter, which characterizes the evolution of the topography is the mean measured AFM height as a function of t_{Ru}, reported in Figure 2. It shows a sharp maximum of 10 nm for a 4 nm nominal thick Ru layer. For layer thickness ranging from zero to 4 nm, the size and height of the Ru patches increase but, as extracted from resistance measurements, they are not connected but separated by regions where the mica substrate is not covered. For layer thickness above 4 nm, those regions are filled in and the maximum AFM height decreases. The patches are then connected leading to a smooth buffer layer above 15 nm. In summary, the 4 nm thick Ru layer is composed by irregular rounded patches separated by non covered mica regions. Their separation by an insulating substrate and their maximum peak to peak height as the optimal corrugation for inducing an isolated Co particle growth were used for producing all Ru/Co structures discussed in this paper.

2.2 Cobalt layer growth

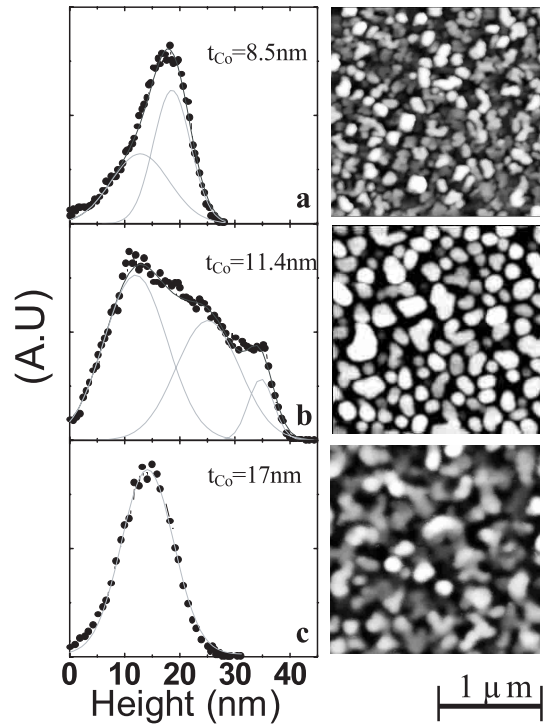The second step in the growth process consists of depositing Co on the 4 nm thick Ru buffer island array.

Fig. 3. Set of AFM topographic images ($2~\mu m \times 2\mu m$ in size) and corresponding height distributions depicting the 3 regimes of the Co growth, for $t_{Co} = 8.5$ nm (a), $t_{Co} = 11.4$ nm (b) and $t_{Co} = 17$ nm (c). The height distributions (solid circles) have been fitted using a combination of Gaussians function indicated in thin lines that correspond to different families of particles.

2.2.1 Topography characterization

In Figure 3, the evolution of the topography of mica/Ru(4 nm)/Co(t_{Co})/Ru(2 nm) stacks is shown as the deposited cobalt thickness t_{Co} is increased. Since the Co layer is capped by a 2 nm thick Ru protecting layer, care must be taken when analyzing the measurements, especially the height of the islands. The thickness of the protecting layer has been optimized, thin to avoid severe alteration of the layer morphology but thick enough to protect the Co layer against oxidation. Despite the Ru capping layer, the AFM images show that the Co growth follows the Ru island structure resulting in Co islands array with an extremely high density.

During the first stage of Co growth ($t_{Co} = 4.5$ nm), the morphology consists of islands with lateral sizes ranging from 60 to 150 nm and interparticle distances of 60–100 nm. The island height follows a narrow Gaussian distribution centered around 12 nm, suggesting thin, disk like shaped Co particles. For Co thicknesses up to 8.5 nm, the morphology does not change significantly although examination of the height distribution in Figure 3a reveals two peaks suggesting the appearance of new Co islands. The interparticle spacing appears to be reduced to 40–80 nm, consistent with the idea of nucleation of new Co particles. The height distribution can be fitted with two Gaussians centered at 12 nm and 18 nm. This bimodal

distribution can be understood if the thicker islands are continuations of the original Ru island growth, while the thinner islands arise from new Co nucleations. This regime of Co island growth will be referred as regime I in the following sections of the paper.

At higher nominal Co thickness (10 nm $< t_{Co} <$ 15 nm) islands of various shapes grow in size laterally as well as vertically. The closest Co islands merge to reach 100–200 nm lateral sizes and spacing of about 100 to 150 nm. An example is shown in Figure 3b for a nominal 11.4 nm thick Co film. At the same time the island's height increases as can be seen in the corresponding height distributions ranging from 10 to 35 nm. This growth regime will be called regime II. The height distribution gives information about the growth process. Height distributions for Co films with thicknesses in regime II (less than 17 nm thick) can be well fitted by using two or three Gaussians, with the lowest in height always being centered at 10–12 nm. All the samples in regime II show similar topography and the most intense peak in the height distribution is located at 12 nm. One or two other peaks are located between 20 and 35 nm. The highest density of small particles in the range of 100 nm lateral size, corresponds to the peak located at 12 nm.

For a critical Co thickness of about 17 nm, regime III occurs. Here the growth process has attained the final stage of continuous film formation, as shown by the height distribution which exhibit only one peak located at 15 nm (Fig. 3c). Additional metal deposition results in coalescence of the nearest islands and at the same time in filling the gap between islands. However, it is difficult to determine when a continuous Co film forms. The problem is an ambiguity in determining the actual thickness of the Co since the AFM tip probes only the island height down to a continuous layer. From AFM alone it is not possible to determine whether the continuous layer is Co or Ru. Nevertheless, together with the magnetic characterization to be described later, a consistent picture has emerged that suggests that, in regime III, a continuous Co layer is formed and only the highest islands remain at the top of the film. The remaining islands have lateral sizes ranging between 200–300 nm. Despite the presence of a continuous cobalt layer, uneven morphologies continue up to 100 nm Co thickness with average height in the range of 25 nm [12,13].

2.2.2 Structural characterization

Nuclear Magnetic Resonance (NMR) experiments have been performed on cobalt layers from the three different growth regimes previously described. NMR is an useful tool to extract the local stacking of atoms in thin layers and especially the proportions of two or more phases when they coexist. A zero field spectrometer technique has been used for this study. The measurements have been performed at 4.2 K and 1.5 K for the thinnest sample, to enhance the signal to noise ratio. The expected frequency positions for a cobalt atom in a bulk hcp environment when the local direction of the magnetization is
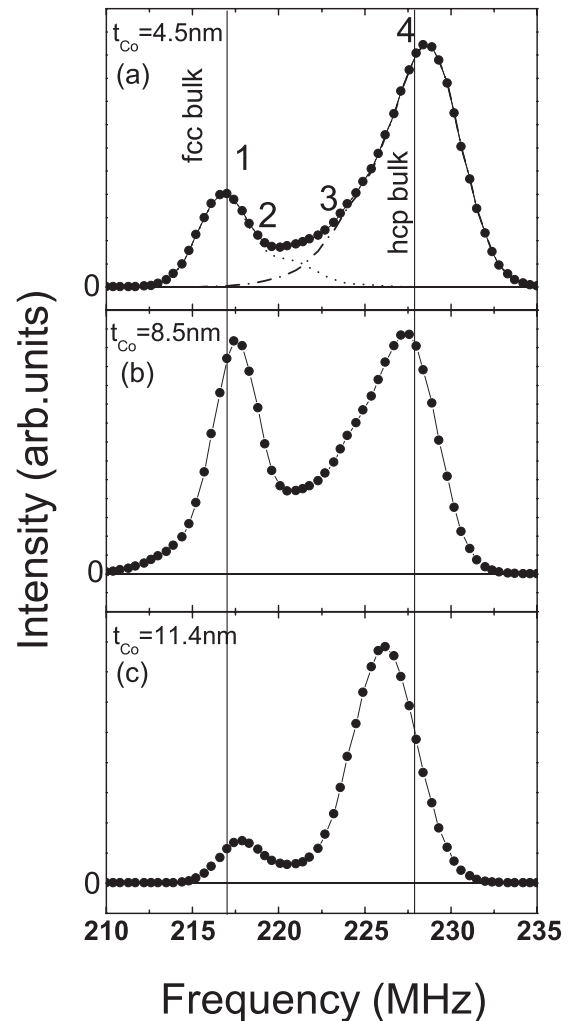

Fig. 4. NMR spectra for Ru(4 nm)/Co(t_{Co})/Ru(2 nm) with (a) $t_{Co} = 4.5$ nm, (b) $t_{Co} = 8.5$ nm and (c) $t_{Co} = 11.4$ nm. An example of decomposition of a NMR spectrum is given in (a). It shows (-) the resultant NMR spectrum, (–) the contribution from the Co atoms in a fcc environment (23% with 8% stacking faults), (-.-) the contribution from Co atoms in hcp environments (77% with 9% stacking faults). The numbers represent the different type of stacking faults as a function of their resonance frequency: (1) fcc, (2) fcc with hcp faults, (3) hcp with fcc faults and (4) hcp.

oriented perpendicular to the c axis (≈ 228 MHz) and for a cobalt atom in a bulk fcc environment (≈ 217 MHz) are indicated. In an hcp environment, the frequency becomes 222 MHz if the local magnetization is parallel to the c axis.

The spectra of the samples with $t_{Co} = 4.5$, 8.5 and 11.4 nm are presented in Figure 4. They show the coexistence of fcc and hcp Co phases in varying proportions. Since the peak attributed to the hcp phase is close to 228 MHz, we can affirm that for those three samples the magnetization direction lies in plane. However, a progressive shift of the hcp phase cobalt peak toward lower frequencies as thickness increases can be due to a part of

Table 1. Proportion of the hcp and fcc phases and stacking faults deduced from the fitted NMR spectra.

Composition	$t_{Co} = 4.5$ nm	$t_{Co} = 8.5$ nm	$t_{Co} = 11.4$ nm
% of hcp Co	77	63	87
% of fcc Co	23	37	13
% of stacking faults in hcp phase	9	14	1
% of stacking faults in fcc phase	8	6	8

magnetization oriented out of the plane. We will demonstrate in the following section that such a magnetization rotation is likely to occur. The goal of those experiments is to obtain quantitative informations about the concentration of cobalt in the hcp and the fcc environment. For this purpose, a model allowing to reproduce the experimental spectrum has been used. This model was developed and tested for Co/Mn multi-layers [18] and cobalt electro-deposited layers [19]. In this model, each spectrum is decomposed in distinct lines as indicated in Figure 4a. Two lines correspond to the hcp ($\approx$ 228 MHz) and fcc ($\approx$ 217 MHz) bulk contributions. Two other lines describe the stacking faults in the hcp and fcc phases. For instance, a fcc stacking fault in hcp bulk appears by an additional line shifted toward lower frequencies. For three successive fcc stacking faults, the corresponding line arises at the bulk fcc position. In order to distinguish the stacking fault's intensities arising from one phase rather than the other one, we make the assumption that the stacking faults are randomly distributed. Three parameters are tunable in this model: the hcp phase fraction (expressed in % of the whole quantity), the hcp stacking fault proportion in the fcc phase (expressed in % of the fcc phase) and the fcc stacking faults proportion in the hcp phase (expressed in % of the hcp phase. Quantitative results are presented in Table 1. It appears that the fcc phase concentration does not decrease when the nominal cobalt thickness is increased as it could be expected if the fcc phase was present at the beginning of the growth. Indeed, the hcp phase concentration is higher for the 4.5 nm nominal cobalt thick layer than for the 8.5 nm.

2.2.3 Discussion of the Co growth

The evolution of the Co structure and morphologies can be understood using the model developed by Campbell [20] to describe the growth of metal on insulating substrates. This model relies on the fact that high mobility metallic atoms incoming on an insulating substrate reduce their energy by climbing previously formed metallic patches. We have used this model to provide a consistent scene of the Co growth on the rough Ru buffer layer, compatible with the informations extracted from the AFM and NMR measurements.

For $t_{Co} = 4.5$ nm, the morphology is composed with 60 nm to 150 nm lateral sized islands. Considering the growth temperature and the height of the thinner Ru/Co islands, Co atoms falling on the mica substrate between Ru islands can overcome the activation barrier to climb up the Ru/Co patches. The growth of the Co islands takes then place preferentially on the Ru islands buffer which favor an hcp structure of Co and a two dimensional growth. However a proportion of Co islands grow directly on the mica substrate, between the highest Ru islands as suggested from the AFM images. Those smaller islands, grown directly on an insulating substrate, are known to have spherical like shape due to the difference of surface energies. So, they exhibit a high surface to volume ratio and have a tendency to crystalize in a fcc phase since it is energetically more favorable to form fcc $\langle 111 \rangle$ faces. As it has been mentioned previously, the particle's size distribution does not change when the Co thickness is increased up to 8.5 nm. However, the density of particles increases. Indeed, the height of the thinner Ru/Co islands has increased as well as the activation barrier the Co atoms have to climb. Therefore, Co atoms on the mica substrate stay on it and form new Co particles with small volumes exhibiting a maximum of fcc $\langle 111 \rangle$ faces. Thus the concentration of atoms in a hcp environment decreases. For higher nominal Co thicknesses, the closest islands merge and the island's lateral size increases (100 to 300 nm), favouring an hcp structure. Thus, the atom's concentration in an hcp environment increases again with the nominal Co thickness and for thicknesses above 11.4 nm, only the hcp phase could be observed.

3 Magnetic properties

Average macroscopic magnetic properties have been investigated using torque magnetometry and AGFM with the field applied either parallel or perpendicular to the film plane. In order to examine domain pattern formation, MFM experiments were also carried out using a *Nanoscope III* system in the tapping/lift mode with a tip magnetized along the tip axis to probe the local magnetic domain structure [14]. For the MFM experiments, the samples were previously demagnetized by sweeping the applied field in plane from positive to negative while decreasing the field [14].

3.1 Hysteresis and magnetic force measurements

In regime I, magnetization curves (*M-H* curves) performed at various temperatures on the 4.5 nm and 8.5 nm Co thick samples gave square loops for the field applied parallel to
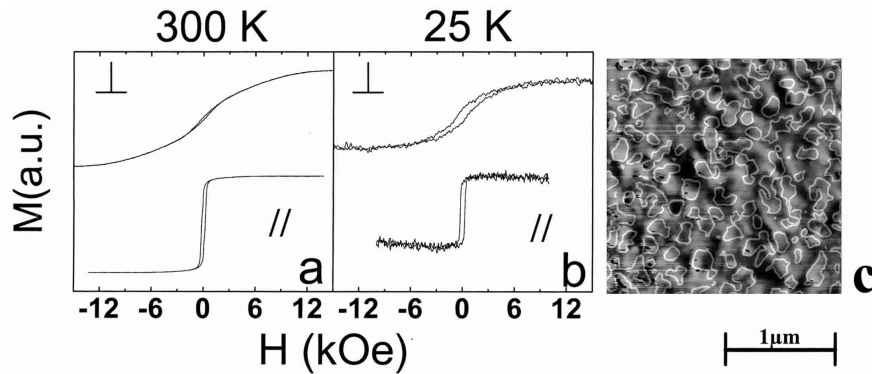
Fig. 5. Perpendicular and parallel magnetization curves performed on a sample with $t_{Co} = 8.5$ nm at 300 K (a) and 25 K (b) typical of samples in regime I. MFM image on the same sample (2 μm $\times$ 2μm in size) obtained at zero field after an in-plane demagnetization (c). The contours of the islands have been stacked on the MFM images in white to show correlation between magnetism and topography.
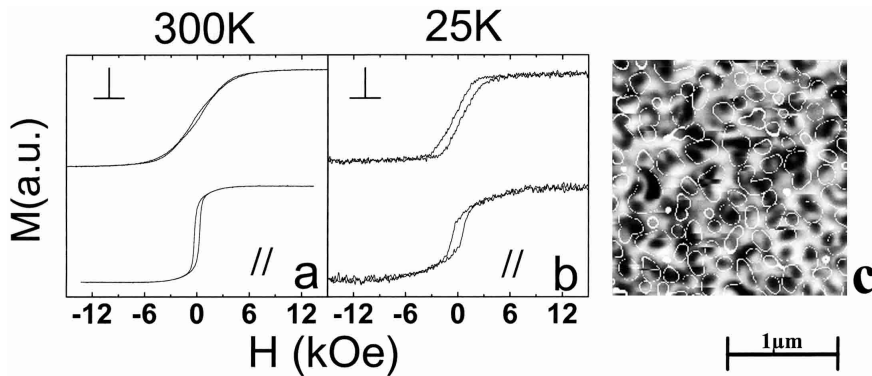

Fig. 6. Perpendicular and parallel magnetization curves performed on a sample with $t_{Co} = 11.4$ nm at 300 K (a) and 25 K (b) typical of samples in regime II. MFM image on the same sample (2 μm $\times$ 2μm in size) obtained at zero field after an in-plane demagnetization (c). The contours of the islands have been stacked on the MFM images in white to show correlation between magnetism and topography.

the film plane. This suggests an in-plane easy axis for both films. This is exemplified in Figure 5a where room temperature parallel and perpendicular M-H curves for the 8.5 nm thick Co film are shown. The saturation field perpendicular to the film plane is equal to 11 kOe at room temperature. At 25 K, an hysteresis appears in the perpendicular M-H curve with a slight increase in the saturation field. A MFM image at room temperature is shown in Figure 5c for this film. Note that MFM images for both samples show diffuse gray contrasts that are not characteristic of magnetic domains with perpendicular magnetization. Moreover for the parallel M-H curve, the saturation field decreases strongly from 6.5 kOe at 300 K to 0.9 kOe at 25 K for the 8.5 nm thick film.

In regime II ($t_{Co} = 9.7$ nm and 11.4 nm) the M-H curves measured at room temperature show that the easy axis remains mainly in plane. Results for the 11.4 nm thick film are given in Figure 6a and b. Interestingly, M-H curves measured at temperatures below 200 K reveal a change of the magnetization easy direction from in plane at 300 K to a direction out of the film plane at 25 K. Further details concerning this reorientation will be discussed in the

next section. The parallelogram shape of the perpendicular curve at 25 K also suggests a reversal of the magnetization in a collection of interacting magnetic particles rather than domain formation in a continuous film [21]. This also supports the picture of regime II as a collection of Co islands rather than a continuous film. The room temperature MFM image measured on the 11.4 nm thick film is shown in Figure 6c. It is difficult to distinguish structures in the MFM contrasts on a scale finer than the smallest particle size determined by AFM. This means that the particles have an in-plane single domain structure. At the same time, a few larger islands exhibit multi-domain structures where the magnetization is perpendicular to the plane or canted. Here the domain structure is clearly dominated by the geometrical constraints of the particle itself. Interestingly, these multi-domain states are very similar to those observed in arrays of square dots [1].

Island shaped films with thickness above 15 nm in regime III display M-H curves that are very similar to those observed for the samples in regime II. An example for a 17 nm thick Co film is shown in Figures 7a and b. However, a close examination of the perpendicular M-H
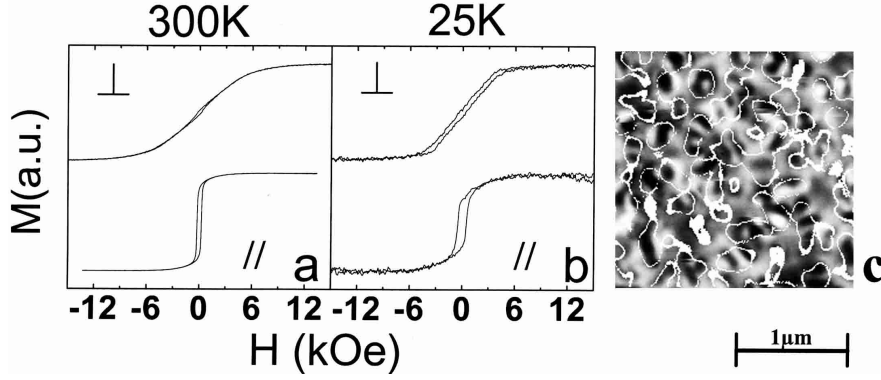
Fig. 7. Perpendicular and parallel magnetization curves performed on a sample with $t_{Co} = 17$ nm at 300 K (a) and 25 K (b) typical of samples in regime III. MFM image on the same sample (2 μm $\times$ 2 μm in size) obtained at zero field after an in-plane demagnetization (c). The contours of the islands have been stacked on the MFM images in white to show correlation between magnetism and topography.

curve at room and at low temperatures reveals an additional contribution at high fields above 7 kOe, represented by a small unsaturated component that signals the presence of a continuous Co layer. The hysteresis which opens in the center of the perpendicular *M-H* curve at room temperature is also narrower than that for the regime II films, as would be expected for a thin film. It is possible that the hysteresis loop for perpendicular magnetization is determined by a combination of Co particles and a continuous film component. The continuous layer would magnetize in-plane with a large saturation field for perpendicular magnetization. These facts are strengthened by the MFM image shown in Figure 7c. It reveals regions that exhibit black and white contrasts of magnetic domains having their magnetization perpendicular to the film plane mainly localized on the islands, and areas with diffuse gray contrasts between the islands where magnetization is still in plane.

3.2 Temperature dependence of anisotropies

Temperature dependent magnetic torque measurements allow an accurate determination of the magnetic anisotropy constants and their temperature dependence. The torque due to an external magnetic applied field was measured as the field was rotated in a plane perpendicular to the film. The 12 kOe applied field was enough to insure a single domain saturated state. The data were fitted using the torque, Γ, calculated from the fourth order expansion of the anisotropy energy, E_a, according to $\Gamma = -\partial E_a / \partial \theta$ where

$$E_a = K_{eff} \sin^2(\theta) + K_2 \sin^4(\theta). \tag{1}$$

Here θ is the angle of the saturation magnetization M_s with respect to the normal of the film plane and K_2 is the fourth order uniaxial magnetocrystalline anisotropy con-
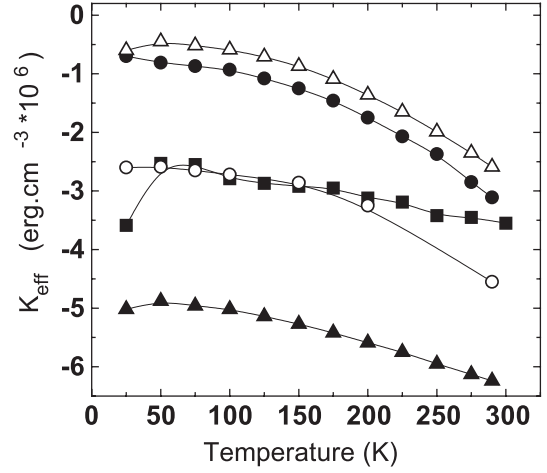

Fig. 8. Temperature dependence of the effective anisotropy constant K_{eff} fitted from the torque curves measured on Co particle-shaped films with nominal thickness of $t_{Co} = 4.5$ nm (solid squares), $t_{Co} = 8.5$ nm (solid triangles), $t_{Co} = 9.7$ nm (solid circles), $t_{Co} = 11.4$ nm (open triangles) and $t_{Co} = 17$ nm (open circles).

stant. The effective anisotropy constant K_{eff} is defined as

$$K_{eff} = K_{MC} + 2\pi M_s^2 \left(N_\parallel - N_\perp \right) \tag{2}$$

where K_{MC} is the second order uniaxial magnetocrystalline anisotropy constant of Co, and $N_\parallel$ and $N_\perp$ are respectively the average particle demagnetization factors along and perpendicular to the substrate. The effective anisotropy constant K_{eff} determined in this manner is reported in Figure 8 as a function of nominal Co thickness and temperature. K_{eff} increases with decreasing temperature for all Co film thicknesses. The thermal behaviors of K_{eff} differs slightly between the different growth regimes while the high order anisotropy, K_2 (not shown) does not show any significant variation with temperature for samples of the three regimes. Its value is equal to

10^6 erg cm^{-3}, in agreement with the measurements of Paige *et al.* [22].

3.2.1 Samples of regimes II and III

For the samples of regimes II and III, the amplitude variation of K_{eff} between room temperature and 25 K is in the order of 2.5×10^6 erg cm^{-3}. This large variation of K_{eff} is the one expected when all the Co layer is stabilized in the hcp structure [22,23]. Indeed, for Co thickness above 10 nm, the layer contains at least 90% of the hcp Co phase. At 300 K however, the value of K_{eff} for regime III samples is nearly twice the value for regime II samples (-2.5×10^6). The observed small differences in hcp Co concentration can not explain the differences of the K_{eff} values between the samples of regime II and III. As a matter of fact, the demagnetizing field energy term $(2\pi M_s^2 (N_\parallel - N_\perp))$ is different for samples in regime II and III. On one hand, for the films in regime III exhibiting a topography composed by a thin continuous Co layer caped by islands, the demagnetizing field energy term is close to that of a continuous layer $-2\pi M_s^2$. On the other hand, for the films in regime II exhibiting a morphology composed by non connected islands, the demagnetizing energy term becomes different from that of a continuous layer as $(N_\parallel - N_\perp)$ is not equal to -1.

3.2.2 Samples of regime I

For the samples in regime I, the amplitude variation of K_{eff} between room temperature and 25 K is weaker ($\approx 10^6$ erg cm^{-3}). The variation of K_{eff} as a function of temperature for samples in regime I can not be due to the thermal variation of an additional term arising from surface anisotropy. Indeed, it has been found that its variation from room temperature to 10 K is in the order of 0.2 erg cm^{-2} for Co films with thickness below 10 nm [24]. However, we have shown in a previous section that samples from regime I exhibit an important mixing of hcp and fcc crystalline phases. The diminution of the K_{eff} variation with temperature suggests then a direct link with the important concentration of the fcc phase. We can thereby interpret the K_{eff} variation using a simple model proposed by Gronkel *et al.* [25]. Within this model, K_{eff} is determined by the relative proportions of hcp and fcc phases:

$$K_{eff} = X K_{MC,hcp} + (1 - X) K_{MC,fcc}$$
$$+ 2\pi M_s^2 (N_\parallel - N_\perp) \quad (3)$$

where X represents the Co proportion in an hcp environment, $K_{MC,hcp}$ is the hcp magnetocristalline anisotropy and $K_{MC,fcc}$ is the fcc magnetocristalline anisotropy. $K_{MC,fcc}$ is in the order of 10^5 erg cm^{-3} and is neglectible compared to the other terms of equation (3). Equation (3) is true if hcp and fcc phases fractions are strongly coupled by exchange interactions or completely uncoupled (*i.e.* well separated hcp and fcc Co islands).
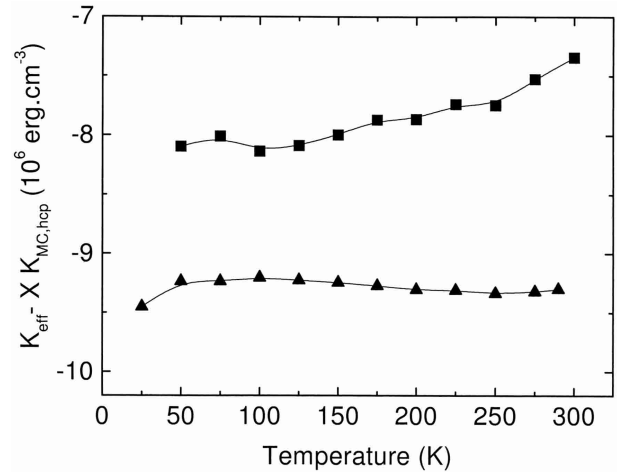

Fig. 9. Thermal variation of $K_{eff} - X K_{MC,hcp}$, measured on Co films with nominal thickness of $t_{Co} = 4.5$ nm (solid squares), $t_{Co} = 8.5$ nm (solid triangles). $K_{MC,hcp}$ is the magnetocristalline anisotropy constant measured on a 10 nm thick continuous hcp Co film.

As a reference, torque measurements on a flat continuous 10 nm thick hcp (0001) Co film deposited on a continuous Ru buffer layer (20 nm thick) were made in order to determine the thermal variation of the bulk $K_{MC,hcp}$ in a thin film. This bulk value was subtracted from the K_{eff} of the particle shaped samples and reported in Figure 9. The result is an experimental determination of $2\pi M_s^2 (N_\parallel - N_\perp) = K_{eff}(T) - X K_{MC,hcp}$ for island-shaped films with $e_{Co} = 4.5$ nm and $e_{Co} = 8.5$ nm.

For the 8.5 nm Co nominal thickness, the Co proportion in a hcp environment is 63% with 14% of stacking faults, so that $X = 54\%$. $K_{eff} - X K_{MC,hcp}$ is almost constant with temperature. Therefore for this film, the diminution of the amplitude variation of K_{eff} is due to the weaker proportion of Co in the hcp phase.

For the thinnest film ($e_{Co} = 4.5$ nm) X is equal to 70%. $K_{eff} - X K_{MC,hcp}$ decreases slighly as the temperature is reduced. For this film, the islands are very tinny with lateral sizes in the order or less then 100 nm. This is still large enough to support bulk like behaviors of K_{MC}. The variation of $K_{eff} - X K_{MC,hcp}$ identified in Figure 9 could then be explained if some islands are superparamagnetic. Some degree of superparamagnetic behavior is also supported by the MFM and AGFM measurements. The MFM images show weak contrasts that could be a sign of random moment orientation. The *M-H* curves show very small hysteresis for the out of plane magnetization but are clearly hysteretic in plane with a small remanence at room temperature. This suggests that the islands are preferentially in plane magnetized and the hysteresis is due to in-plane effective anisotropies.

In the superparamagnetic case, M_s in equation (3) should be replaced by M, the mean magnetization, and the reduction of $K_{eff} - X K_{MC,hcp}$ with temperature is attributed to the reduction of the magnetic moment fluctuation of the smaller volume particles when temperature is decreased. For small non-interacting uniaxial particles,

a blocking temperature below which the magnetization is frozen can be estimated by:

$$T_B = K_{\text{eff}}V/25k_b. \qquad (4)$$

Since the variation of $K_{\text{eff}} - XK_{\text{MC,hcp}}$ for the 4.5 nm thick film seems more significant for temperature above 200 K, a blocking temperature of 200 K was roughly estimated. From equation (4), those particles have a volume above 230 nm^3 but smaller than the mean volume measured from the AFM images. Using this volume value, we were however able to simulate the in plane and out of plane *M-H* curves using a modified Langevin function including the effect of the anisotropy. From the AFM measurements, there are several size distributions contributing to the overall magnetic properties of these samples. This means that any superparamagnetic contribution arising from particles with very small volumes will be superimposed to ferromagnetic contributions arising from particles with larger volumes.

4 Magnetic re-orientation

In a single domain state, the easy axis of magnetization for Co thicknesses lower than 8.5 nm, addressed as regime I of growth, are in plane for temperature ranging from 300 K to 25 K. However, the samples with thicknesses ranging from 9 to 15 nm (regime II) show an interesting feature that is not seen for the thinnest films. The regime II films show a magnetization reorientation from an in-plane to an out-of-plane direction at low temperature.

The prime evidence for this magnetization reorientation comes from the torque curves. Data taken on the 11.4 nm Co thick samples are presented in Figure 10. The re-orientation is signaled by the appearance of two additional angles for which the torque vanishes when temperature is decreased below 200 K. These angles different from 0° and 90° show that the preferred orientation is neither in plane nor out-of-plane. Instead, the magnetization prefers to orient along a cone, defined by the angle where the additional zeroes from the torque curves appear. This angle can also be calculated from the measured values of K_{eff} and K_2 by minimizing the energy E_a given in equation (1). The stable solutions for nonzero θ that minimize E_a are $0 > K_{\text{eff}} > -2K_2$. The corresponding cone angle θ_c is:

$$\theta_c = \arcsin\left[\sqrt{(-K_{\text{eff}}/2K_2)}\right]. \qquad (5)$$

As $K_2 = 10^6$ erg cm^{-3} and from Figure 8, it can be seen that the required conditions on K_{eff} and K_2 are only satisfied at low temperatures (lower than 200 K). The formation of a cone orientation is determined by the thermal variation of K_{eff}, which is the most sensitive to temperature. The values of the cone angle *versus* temperature are given in Figure 11 for $t_{\text{Co}} = 9.7$ nm and 11.4 nm. There
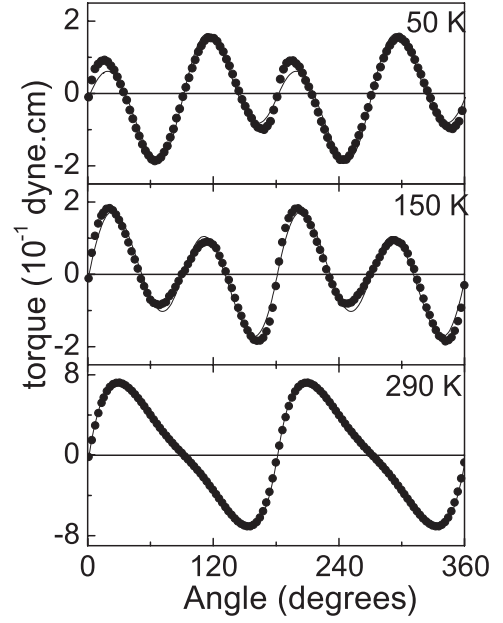

Fig. 10. Measured and calculated torque curves performed at different temperature as a function of the angle between the applied field and the perpendicular to the sample for $t_{\text{Co}} = 11.4$ nm. The measured data appears as solid circles. The calculated values (assuming that magnetization and field are collinear) are given by the solid lines.
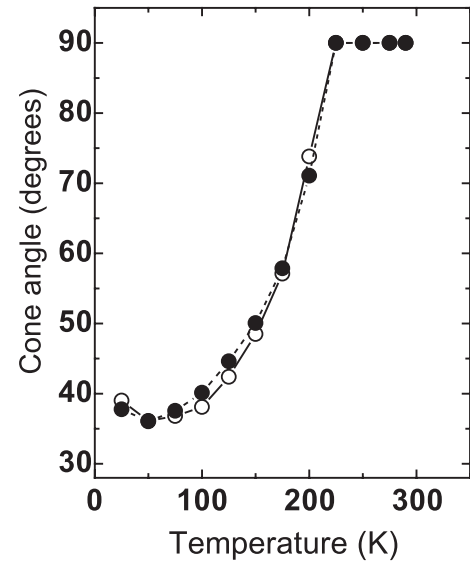

Fig. 11. Measured and calculated cone angles θ_c as a function of temperature for $t_{\text{Co}} = 11.4$ nm. The measured values (open circles) were determined from the additional zeros in the torque measurements and the calculated values (solid circles) were found using the fitted anisotropy values.

is a good agreement between the measured and the calculated value of θ_c. The room temperature in-plane magnetization switches to angles of 45° and 53° respectively for temperatures below 200 K. Such behavior has been previously observed in submicronic cobalt dots fabricated by lithography [23]. The reorientation here, as in the case of the dots, is driven by the large thermal variation of

K_{eff} together with the particular shape anisotropy of the small particle geometry. The observation of the cone angle reorientation in the films examined here supports the argument that the samples are primarily composed of separated small Co particles.

5 Conclusion

The growth of thin Ru and Co films has been studied in growth regimes favouring islanding of Co and Ru. Control of the islanding was achieved in such a way that isolated Co particles were formed on Ru island substrates. The distribution of sizes and spacing of these particles is remarkably narrow, and the technique may hold promise as a relatively simple mean of producing very small Co particles.

The growth of the Ru and Co islands was found to follow different steps leading to the formation of a continuous film. It was found that even after the formation of a continuous film, the islands continue to develop. The island growth and consequent effects on magnetic properties were studied in detail using magnetometry and magnetic force microscopy. Correlations were found between the magnetic properties and island formation process. For each growth regime, particular structural and magnetic characteristics were observed.

The magnetic properties were found to be strongly affected by the island shape. One of the consequences of the interplay between particle shape, size and the thermal variations of the anisotropies is the possibility of reorientation transitions. An out-of-plane reorientation, observed earlier in patterned Co magnetic dots, was found for low temperatures in the films grown in the second regime. The existence of this transition provides further evidence that some of the growth regimes are characterized by the formation of narrow distributions of small magnetic particles.

References

1. M. Hehn, K. Ounadjela, J.-P. Bucher, F. Rousseaux, D. Decanini, B. Bartenlian, C. Chappert, Science **272**, 1782 (1996).
2. P.R. Krauss, P.B. Fischer, S.Y. Chou, J. Vac. Sci. Technol. B **12**, 3639 (1994).
3. R.M.H. New, R.F.W. Pease, R.L. White, J. Vac. Sci. Technol. B **12**, 3196 (1994).
4. H.J. Elmers, J. Hauschild, H. Höche, U. Gradman, H. Berhge, D. Heuer, U. Khöler, Phys. Rev. Lett. **73**, 898 (1994).
5. J. Hauschild, H.J. Elmers, U. Gradman, Phys. Rev. B **57**, R677 (1998).
6. H. Brune, M. Giovannini, K. Bromann, K. Kern, Nature **394**, 451 (1998).
7. B. Voigtländer, G. Meyer, N.M. Amer, Phys. Rev. B **44**, 10354 (1991).
8. O. Fruchart, M. Klaua, J. Barthel, J. Kirschner, Phys. Rev. Lett **83**, 2769 (1999).
9. L. Piraux, J.M. Georges, J.F Despres, C. Leroy, E. Ferain, R. Legras, K. Ounadjela, A. Fert, Appl. Phys. Lett. **65**, 2484 (1994).
10. A. Sugawara, G.G. Hembree, M.R. Scheinfein, J. Appl. Phys. **82**, 5662 (1997).
11. S. Ohnuma, Y. Nakanouchi, C.D. Graham, T. Masumoto, IEEE Trans. Mag. **21**, 2038 (1985).
12. M. Demand, M. Hehn, S. Cherifi, K. Cherifi, K. Ounadjela, R.L. Stamps, IEEE Trans. Magn. **34**, 1084 (1998).
13. J.-V. Kim, M. Demand, M. Hehn, K. Ounadjela, R.L. Stamps, Phys Rev. B **62**, 6467 (2000).
14. M. Hehn, S. Padovani, K. Ounadjela, J.P. Bucher, Phys Rev. B **54**, 3428 (1996).
15. A. Arbaoui, Ph.D. thesis, University of Strasbourg (1993); Y. Henry, A. Michel, Ph.D. thesis, University of Strasbourg (1995); M. Hehn, Ph.D. thesis, University of Strasbourg (1997).
16. D.W. Pashley, M.J. Stowell, M.H. Jacobs, T.J. Law, Philos. Mag. **10**, 127 (1964).
17. A.A. Baski, H. Fuchs, Surf. Sci. **313**, 275 (1994).
18. V. Pierron-Bohnes, A. Michel, J.P. Jay, P. Panissod, Mat. Res. Soc. Symp. Proc. **528**, 169 (1998).
19. J.L. Bubendorff, C. Meny, E. Beaurepaire, P. Panissod, J.P. Bucher, Eur. Phys. J. B **17**, 635 (2000).
20. C.T. Campbell, Surf. Sci. Rep. **27**, 1 (1997).
21. W. Andrä, H. Danan, IEEE Trans. Mag. **20**, 102 (1984).
22. D.M. Paige, B. Spuznar, B.K. Tanner, J. Magn. Magn. Mater. **44**, 239 (1984).
23. M. Hehn, K. Ounadjela, R. Ferré, W. Grange, Appl. Phys. Lett. **71**, 2833 (1997).
24. C. Chappert, K. Le Dang, P. Beauvillain, H. Hurdequint, D. Rennard, Phys. Rev. B **34**, 3192 (1986).
25. H.A.M. Gronkel, P.J.H. Bloeman, E.A.M. van Alphen, W.J.M. de Jonge, Phys. Rev. B **49**, 11327 (1994).
26. R.W. Chantrell, N.S. Walmsley, J. Gore, M. Maylin, J. Appl. Phys. **85**, 4340 (1999).
27. F. Atamny, A. Baiker, Surf. Sci. **401**, 227 (1998).
28. S.M. Jordan, R. Schad, A.M. Keen, M. Biscohoff, D.S. Schmool, H. van Kempen, Phys. Rev. B. **59**, 7350 (1999).
29. G.W. Crabtree, Phys. Rev. B **16**, 1117 (1977).